



# Turbulence in the Local Interstellar Medium and the *IBEX* Ribbon

E. J. Zirnstein<sup>1</sup> , J. Giacalone<sup>2</sup>, R. Kumar<sup>1</sup> , D. J. McComas<sup>1</sup> , M. A. Dayeh<sup>3</sup> , and J. Heerikhuisen<sup>4,5</sup>

<sup>1</sup> Department of Astrophysical Sciences, Princeton University, Princeton, NJ 08544, USA; [ejz@princeton.edu](mailto:ejz@princeton.edu)

<sup>2</sup> Department of Planetary Sciences, University of Arizona, Tucson, AZ 85721, USA

<sup>3</sup> Southwest Research Institute, San Antonio, TX 78228, USA

<sup>4</sup> Department of Mathematics and Statistics, University of Waikato, Hamilton, New Zealand

<sup>5</sup> Department of Space Science, University of Alabama in Huntsville, Huntsville, AL 35899, USA

Received 2019 May 31; revised 2019 November 18; accepted 2019 November 18; published 2020 January 3

## Abstract

The effects of turbulence in the very local interstellar medium (VLISM) have been proposed by Giacalone & Jokipii to be important in determining the structure of the *Interstellar Boundary Explorer* (*IBEX*) ribbon via particle trapping by magnetic mirroring. We further explore this effect by simulating the motion of charged particles in a turbulent magnetic field superposed on a large-scale mean field, which we consider to be either spatially uniform or a draped field derived from a three-dimensional magnetohydrodynamic simulation. We find that the ribbon is not double-peaked, in contrast to Giacalone & Jokipii. However, the magnetic mirror force still plays an important role in trapping particles. Furthermore, the ribbon is considerably thicker if the large-scale mean field is draped around the heliosphere. *Voyager 1* observations in the VLISM show a turbulent field component that is stronger than previously thought, which we test in our simulation. We find that the inclusion of turbulent fluctuations at scales  $\gtrsim 100$  au and power consistent with *Voyager 1* observations produces a ribbon whose large-scale structure is inconsistent with *IBEX* observations. However, restricting fluctuations to  $< 100$  au produces a smoother ribbon structure similar to *IBEX* observations. Different realizations of turbulence produce different small-scale features ( $\lesssim 10^\circ$ ) in the ribbon, but its large-scale structure is robust if the maximum fluctuation size is  $\lesssim 50$  au. This suggests that the magnetic field structure at scales  $\lesssim 50$  au is determined by the heliosphere–VLISM interaction and cannot entirely be represented by pristine interstellar turbulence.

*Unified Astronomy Thesaurus concepts:* Heliosphere (711); Pickup ions (1239); Solar wind (1534); Interstellar medium (847); Interstellar magnetic fields (845); Particle physics (2088); Interplanetary turbulence (830)

## 1. Introduction

The supersonic solar wind (SW) plasma, consisting mostly of protons, electrons, and a few percent alpha particles, flows radially away from the Sun typically at speeds from  $\sim 300$  to  $800 \text{ km s}^{-1}$ . The SW slows down to subsonic speeds at the termination shock ( $\sim 100$  au from the Sun), and the subsonic SW interacts with the partially ionized interstellar gas in the very local interstellar medium (VLISM), forming the heliosphere with a tangential discontinuity (i.e., the heliopause) that separates the solar and interstellar plasmas (e.g., Zank 1999, 2015). The neutral matter from the interstellar medium can cross the heliopause and travel into the inner heliosphere. Moreover, interstellar neutral atoms, mostly hydrogen and helium, can charge-exchange with SW ions, generating “pickup ions from neutral interstellar wind” (PINI) as well as energetic neutral atoms (ENAs), which can propagate large distances before ionizing.

The *Interstellar Boundary Explorer* (*IBEX*; McComas et al. 2009a) is an Earth-orbiting spacecraft with two single-pixel cameras (Funsten et al. 2009; Fuselier et al. 2009) that detect interstellar neutral atoms flowing into the heliosphere from the VLISM (e.g., Möbius et al. 2009; McComas et al. 2015; Kubiak et al. 2016; Park et al. 2016; Schwadron et al. 2016; Bzowski et al. 2017) and ENAs produced by charge-exchange in the outer heliosphere (e.g., McComas et al. 2009b, 2017, 2018b; Schwadron et al. 2018; Desai et al. 2019). Full-sky observations of neutral atoms provide a means to deduce the thermodynamic and structural properties of the outer

heliosphere and its interaction with the VLISM (e.g., Bzowski et al. 2017; Zirnstein et al. 2017).

*IBEX* discovered an unpredicted enhancement of ENAs, called the “ribbon,” forming a nearly complete circle across the celestial sky (McComas et al. 2009b); these authors also showed that the ribbon may contain fine-scale structure. This ribbon of enhanced ENAs has been measured and studied ever since its discovery in 2009. The ribbon flux is strongly correlated with the local interstellar magnetic field (ISMF) draped around the heliosphere (Schwadron et al. 2009; Heerikhuisen & Pogorelov 2011; Pogorelov et al. 2011; Zirnstein et al. 2016), and it is believed to be formed from “secondary” ENAs produced by charge-exchange between “pickup ions from neutral solar wind” (PINS) and interstellar neutral atoms in the draped ISMF outside the heliopause (e.g., McComas et al. 2009b, 2017; Zirnstein et al. 2015a). Numerous models have furthered our understanding of the ribbon’s origin from the secondary ENA mechanism (e.g., Chalov et al. 2010; Gamayunov et al. 2010; Heerikhuisen et al. 2010; Möbius et al. 2013; Schwadron & McComas 2013; Isenberg 2014, 2015; Giacalone & Jokipii 2015, hereafter GJ15; Zirnstein et al. 2018), focusing our attention on whether or not the parent PINS experience significant pitch angle scattering outside the heliopause (e.g., Florinski et al. 2010, 2016; Summerlin et al. 2014; Niemiec et al. 2016), whether the interstellar turbulence is important (GJ15; Gamayunov et al. 2017, 2019), how different extremes of pitch angle scattering affect the ribbon flux observed at 1 au (e.g., Zirnstein et al. 2018, 2019; Gamayunov et al. 2019), and how the ribbon’s

source distribution and the  $\mathbf{B} \cdot \mathbf{r} = 0$  surface are related to the draping of the ISMF around the heliosphere (e.g., Grygorczuk et al. 2011; Strumik et al. 2011; Ratkiewicz et al. 2012; Isenberg et al. 2015; Zirnstein et al. 2015a, 2016).

One of the possible sources of the *IBEX* ribbon is the interaction between PINS and interstellar turbulence (GJ15). These authors showed that the propagation of PINS in the presence of homogeneous turbulence with a uniform mean magnetic field in the VLISM can produce a ribbon of width  $\sim 10^\circ$  due to a magnetic mirror force that traps particles with high pitch angles near  $\mathbf{B} \cdot \mathbf{r} = 0$ . GJ15 also predict that this causes the ribbon emission to have a double-humped flux profile perpendicular to the ribbon; however, we have found this to be a numerical artifact of the method they used and not real, as we discuss further below. But an important question remains: what does the ribbon observed at 1 au look like when there is interstellar turbulence and the ISMF is draped around the heliosphere? Moreover, recent *Voyager 1* observations of turbulence in the VLISM suggest that the level of turbulence at length scales  $< 5$  au is much larger than the estimated interstellar turbulence at this scale (Burlaga et al. 2018). Then the question arises: how does this greater power in the turbulent fluctuations affect the ribbon?

In this study, we implement the model presented by GJ15, namely the propagation of PINS in the presence of turbulence outside the heliopause. We extend the work of GJ15 by including a homogeneous magnetic turbulent component that is superposed on a mean field derived from a three-dimensional (3D) magnetohydrodynamic (MHD) simulation of the heliosphere. The 3D MHD simulation models the draping of the large-scale ISMF around the heliopause. We present the model assumptions in Section 2, present results of simulated ENA fluxes at 1 au in Section 3, and discuss their implications for the origin of the *IBEX* ribbon and turbulence in the VLISM in Section 4.

## 2. Model

### 2.1. Simulation of the Heliosphere

Similar to our earlier work on modeling the ribbon (e.g., Zirnstein et al. 2018, 2019), we utilize plasma and neutral results from a 3D global simulation of the SW-VLISM interaction. The simulation iterates between MHD-plasma and kinetic (Boltzmann)-neutral modules, coupled by energy-dependent, charge-exchange source terms, to simulate the heliosphere (e.g., Pogorelov et al. 2008, 2009a; Heerikhuizen et al. 2009, 2013). The VLISM boundary conditions, applied at a radius of 1000 au from the Sun, were derived based on constraining the *IBEX* ribbon's position in the sky (Zirnstein et al. 2016), producing an ISMF magnitude of  $2.93 \mu\text{G}$  and direction ( $227^\circ 28$ ,  $34^\circ 62$ ) in ecliptic J2000 coordinates at the outer boundary of the simulation (1000 au). This field produces a draped magnetic field at the location of *Voyager 1* that is consistent with its measurements of the field magnitude and orientation. The interstellar neutral temperature ( $7500 \text{ K}$ , assumed to be the same for ions), flow speed ( $25.4 \text{ km s}^{-1}$ ), and inflow direction ( $255^\circ 7$ ,  $5^\circ 1$ ) are derived from *IBEX* observations of interstellar neutral atoms (McComas et al. 2015). With these boundary conditions and an interstellar plasma density of  $0.09 \text{ cm}^{-3}$  and neutral hydrogen density of  $0.154 \text{ cm}^{-3}$ , the simulation is also consistent with (1) the distance to the heliopause in the directions to *Voyager 1*

(Stone et al. 2013; Gurnett et al. 2013) and *Voyager 2*<sup>6</sup> ( $\sim 120$  au from the Sun), (2) the correlation between the deflection plane of interstellar neutral hydrogen (Lallement et al. 2010) and the plane formed by the ISMF direction ( $\mathbf{B}$ ) and the VLISM inflow direction ( $\mathbf{V}$ ), i.e., the  $\mathbf{B}-\mathbf{V}$  plane (Zirnstein et al. 2016), and (3) the interstellar neutral hydrogen density at the termination shock near the VLISM inflow direction ( $\sim 0.1 \text{ cm}^{-3}$ ; Bzowski et al. 2009).

The SW boundary conditions at 1 au are the same as those used in our previous work: SW plasma density is  $5.74 \text{ cm}^{-3}$ , plasma temperature is  $51,100 \text{ K}$ , flow speed is  $450 \text{ km s}^{-1}$ , and the radial component of magnetic field in the Parker spiral is  $37.5 \mu\text{G}$ . The SW values are advected to the simulation's inner boundary (10 au) by adiabatic expansion. The SW boundary conditions are assumed to be independent of time and latitude. Moreover, to avoid the artificial presence of a flat current sheet and spurious magnetic reconnection at the heliopause that may arise due to numerical dissipation, SW magnetic field in this study is unipolar.

### 2.2. The Neutralized SW

We create a neutralized SW distribution as the source of PINS outside the heliopause following Swaczyna et al. (2016b) and Zirnstein et al. (2019). We utilize results from a model of the SW speed and density derived from interplanetary scintillation (IPS) observations as a function of heliographic latitude (Sokół et al. 2015). We average SW speed and density at 1 au ( $u_{\text{SW},0}$  and  $n_{\text{SW},0}$ , respectively) over time from 2000 through 2009, which accounts for (1) the predicted  $\sim 4-9$  yr delay between SW observations at 1 au and *IBEX* ribbon observations at 1 au (Zirnstein et al. 2015b) and (2) the time-averaged, first five years of *IBEX* observations from 2009 to 2013 (McComas et al. 2014), which we compare to later in the paper. Thus, the neutralized SW differential flux,  $I_{\text{NSW}}$ , at the radial distance of the termination shock,  $r_{\text{TS}}$  (which we assume to be 100 au), is given by (e.g., Swaczyna et al. 2016b)

$$I_{\text{NSW}}(r_{\text{TS}}, v, \theta) = \frac{1}{M} \sum_i \int_{r_0}^{r_{\text{TS}}} [n_{\text{SW},0}(\theta, i) u_{\text{SW},0}(\theta, i)] \left( \frac{r_0}{r_{\text{TS}}} \right)^2 \times [n_{\text{H}} \sigma_{\text{ex}}(v)] e^{-n_{\text{H}} \sigma_{\text{ex}}(v) r} N(u_{\text{SW},i}(r), \delta v | v) \frac{1}{m_p v} dr, \quad (1)$$

where  $v$  is the neutral SW speed,  $\theta$  is the heliographic latitude,  $i$  is the Carrington rotation number summed over 1958 through 2009 (total  $M = 134$ ),  $r_0 = 1 \text{ au}$ ,  $n_{\text{H}} = 0.09 \text{ cm}^{-3}$  is the interstellar neutral hydrogen density in the supersonic SW (e.g., Bzowski et al. 2009),  $\sigma_{\text{ex}}$  is the energy-dependent, charge-exchange cross section (Lindsay & Stebbings 2005),  $r$  is the radial distance from the Sun,  $m_p$  is the proton mass, and  $N$  is a Gaussian speed distribution with mean speed  $u_{\text{SW},i}(r)$  and thermal speed  $\delta v = 100 \text{ km s}^{-1}$  that smooths the SW in speed (Swaczyna et al. 2016b). The SW slows down farther from the Sun due to mass-loading from PINI. This effect is

<sup>6</sup> [https://voyager.jpl.nasa.gov/news/details.php?article\\_id=112](https://voyager.jpl.nasa.gov/news/details.php?article_id=112)

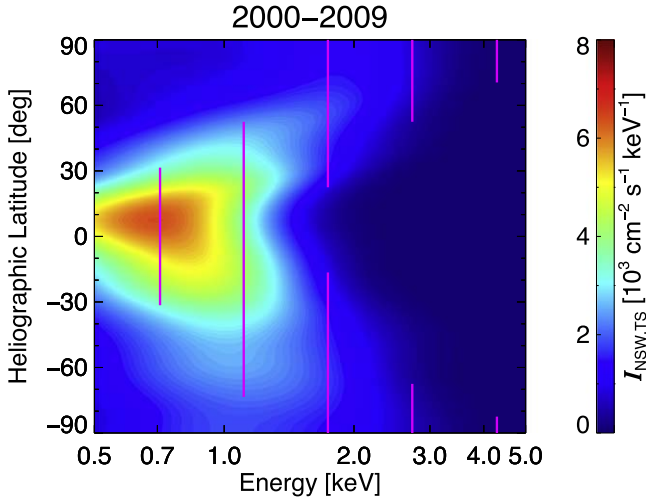


**Figure 1.** Neutral SW flux at the termination shock,  $I_{\text{NSW,TS}}$ , as a function of energy and heliographic latitude. We show data time-averaged from 2000 through 2009, which approximately corresponds to the observation time of *IBEX* from 2009 to 2013. The magnetic lines show the central energies of the *IBEX-Hi* energy channels, with ranges in latitude that cover fluxes greater than half of the maximum at that energy.

approximated by (e.g., Lee et al. 2009)

$$u_{\text{SW}}(r) = u_{\text{SW},0} \left[ 1 - \left( 1 - \frac{1}{2} \frac{\gamma - 1}{2\gamma - 1} \right) \frac{r}{\lambda_{\text{ml}}} \right],$$

$$\lambda_{\text{ml}} = \left[ n_{\text{H}} \sigma_{\text{ex}} + \frac{\nu_{\text{H}} n_{\text{H}} + 4\nu_{\text{He}} n_{\text{He}}}{n_{\text{SW},0} u_{\text{SW},0}} \right]^{-1}, \quad (2)$$

where  $\gamma = 5/3$  is the adiabatic index,  $n_{\text{He}} = 0.015 \text{ cm}^{-3}$  is the interstellar neutral helium density in the supersonic SW (Gloeckler et al. 2004), and  $\nu_{\text{H}} = \nu_{\text{He}} = 10^{-7} \text{ s}^{-1}$  are the photoionization rates for hydrogen and helium atoms, respectively, at 1 au (Bzowski et al. 2013; Sokół et al. 2019). Integrating Equation (1) to  $r_{\text{TS}}$  gives the SW differential flux at the SW termination shock, averaged from 2000 through 2009, which is plotted in Figure 1 (for more details, see Swaczyna et al. 2016b; Zirnstein et al. 2019).

To compute the neutral SW flux outside the heliopause, we account for (1) the  $r^{-2}$  expansion of the neutral SW and (2) the loss by charge-exchange in the outer heliosheath. Thus, the neutral SW differential flux at distance  $r$  from the Sun (here,  $r > r_{\text{HP}}$ ) is

$$I_{\text{NSW}}(\mathbf{r}, \nu) = I_{\text{NSW}}(r_{\text{TS}}, \nu, \theta) \left( \frac{r_{\text{TS}}}{r} \right)^2 e^{-\int_{r_{\text{HP}}}^r n_{\text{p}}(r') \sigma_{\text{ex}} dr'}. \quad (3)$$

### 2.3. Turbulent Magnetic Field

Following Giacalone & Jokipii (1999), we construct a 3D turbulent magnetic field component by superimposing a large number of shear Alfvén waves of random polarizations, phases, and wavevector directions. For a large enough number of wave modes, this method yields an isotropic and spatially homogeneous turbulent field (Batchelor 1960). The random component of the magnetic field,  $\delta \mathbf{B}$ , is (see also

Giacalone & Jokipii 1999 for more details)

$$\delta \mathbf{B}(x, y, z) = \sum_{n=1}^{N_{\text{m}}} A(k_n) \hat{\xi}_n \exp(ik_n z'_n + i\beta_n), \quad (4)$$

$$\hat{\xi}_n = \cos \alpha_n \mathbf{x}'_n + i \sin \alpha_n \mathbf{y}'_n, \quad (5)$$

$$\begin{pmatrix} x' \\ y' \\ z' \end{pmatrix} = \begin{pmatrix} \cos \theta_n \cos \varphi_n & \cos \theta_n \sin \varphi_n & -\sin \theta_n \\ -\sin \varphi_n & \cos \varphi_n & 0 \\ \sin \theta_n \cos \varphi_n & \sin \theta_n \sin \varphi_n & \cos \theta_n \end{pmatrix} \begin{pmatrix} x \\ y \\ z \end{pmatrix}, \quad (6)$$

where  $n$  is the wave mode number out of a total  $N_{\text{m}}$ ,  $k_n$  is the wavenumber,  $\alpha_n$  is the polarization,  $\beta_n$  is the phase, and the propagation direction of each wave mode is represented by angles  $\theta_n$  and  $\varphi_n$ . For isotropic turbulence,  $\alpha_n$ ,  $\beta_n$ ,  $\theta_n$ , and  $\varphi_n$  are selected randomly from a uniform distribution in the following ranges:  $0 < \alpha_n < 2\pi$ ,  $0 < \beta_n < 2\pi$ ,  $-1 < \cos(\theta_n) < 1$ , and  $0 < \varphi_n < 2\pi$ . For the results presented in this study we set  $N_{\text{m}} = 500$ .

The wave amplitude  $A(k_n)$  is represented by a Kolmogorov spectrum, such that

$$A^2(k_n) = \sigma^2 G(k_n) / \left[ \sum_{n=1}^{N_{\text{m}}} G(k_n) \right], \quad (7)$$

$$G(k_n) = \frac{4\pi k_n^2 \Delta k_n}{1 + (k_n L_c)^\gamma}, \quad (8)$$

where  $\gamma = 11/3$  for a 3D Kolmogorov spectrum and  $\sigma^2$  is the wave variance. Similar to Giacalone & Jokipii (1999), the logarithms of wavenumbers are equally spaced.

Following GJ15, for each simulation presented in this study, we construct a turbulence spectrum with an upper limit scale of 20 pc and a lower limit scale of  $0.5 \times r_{\text{g}}$ , where  $r_{\text{g}}$  is the gyroradius of a  $400 \text{ km s}^{-1}$  proton in a  $4 \mu\text{G}$  magnetic field. A lower limit of  $0.5 \times r_{\text{g}}$  is sufficient to simulate the effects of magnetic mirroring and particle interactions with waves of the order of the gyroradius. We have tested that including smaller wave modes requires a much longer runtime but does not significantly change the effects of magnetic mirroring due to the smaller wave power at smaller scales. Setting the lower limit scale to a larger wavelength would improve runtime efficiency but would not include wave modes that may cause pitch angle scattering. While setting the lower limit to  $0.5 \times r_{\text{g}}$  may not simulate the effects of pitch angle scattering completely, we find it is a sufficient compromise between accuracy and computational efficiency. The total magnetic field is given by  $\mathbf{B}(x, y, z) = \mathbf{B}_0(x, y, z) + \delta \mathbf{B}(x, y, z)$ , where  $\mathbf{B}_0$  is the mean magnetic field. For the majority of the results presented in this study, we set  $\mathbf{B}_0$  equal to the magnetic field from our 3D MHD simulation of the heliosphere's interaction with the VLISM ( $\mathbf{B}_{\text{MHD}}$ ; e.g., Pogorelov et al. 2009b; Heerikhuisen et al. 2014; Zirnstein et al. 2016). Since we desire the total mean field to be dominated at large scales ( $\gtrsim 100 \text{ au}$ ) by the draped MHD field, when summing over wave modes at each iteration of the particle stepping, we integrate up to a cutoff scale similar to or smaller than the scale size of the heliosphere.

An analytic expression for the 1D Kolmogorov turbulent power spectrum, which we use to plot the power spectrum in



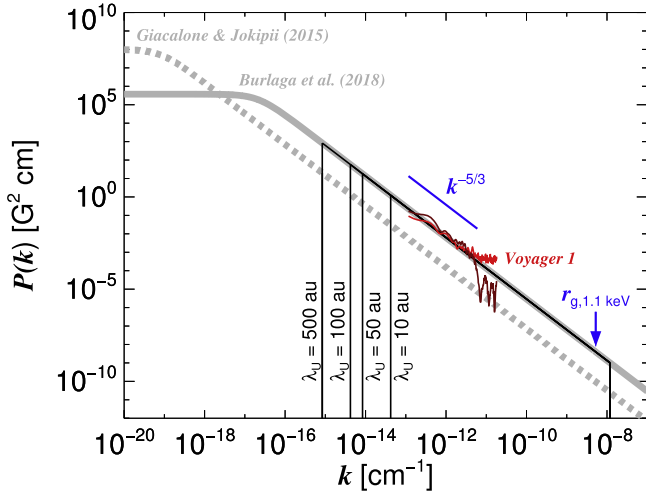


**Figure 2.** Kolmogorov power-law spectra with different parameters used in this study. Theoretical spectra (solid/dashed gray and black curves) are calculated using Equation (9). The power spectrum similar to that used by GJ15 is shown as the dashed gray curve ( $L_C = 4$  pc,  $\sigma_C = 4$   $\mu$ G), and the power spectrum similar to Burlaga et al. (2018) required to match the *Voyager 1* observations is shown as the solid gray curve ( $L_C = 0.015$  pc,  $\sigma_C = 4$   $\mu$ G). We show *Voyager 1* data from Burlaga et al. (2018) for time periods 2013.3593–2014.6373 (dark red) and 2015.3987–2016.6759 (light red). The scale of a proton gyroradius ( $r_g$ ) with energy 1.1 keV, equivalent to the central energy of the *IBEX-Hi* energy passband 3 (Funsten et al. 2009), in a 4  $\mu$ G magnetic field is shown by the blue arrow. We simulate the ribbon in turbulence spectral cutoff scales (wavelength upper limit,  $\lambda_U$ ), with a minimum wavelength of  $\sim 0.5 \times r_{g,1.1\text{keV}}$ .

Figure 2, is given by (e.g., Appendix B in Giacalone & Jokipii 1999)

$$P(k) = \frac{\frac{\sigma^2}{1 + (kL_C)^{5/3}}}{\int_0^\infty \frac{dk}{1 + (kL_C)^{5/3}}} = \frac{5 \sin(3\pi/5)}{3\pi} \frac{\sigma^2 L_C}{1 + (kL_C)^{5/3}}. \quad (9)$$

We note that the expression used by Burlaga et al. (2015, 2018) is different than our Equation (9) by a factor of 2 because they integrate over wavenumbers from  $-\infty$  to  $\infty$  and replace  $k$  with  $|k|$  in Equation (9). We use the form of Equation (9) presented here to clarify that  $k$  is the magnitude of the wavevector and must be positive; therefore,  $k$  is integrated from 0 to  $\infty$ .

#### 2.4. Solving Particle Motion

Following GJ15, we numerically integrate the equation of motion for protons in a turbulent magnetic field outside the heliopause. However, in this study we define the heliopause surface using the MHD simulation. The motion of protons in a magnetic field is governed by the Lorentz force equation (written in non-relativistic form, in cgs units),

$$\frac{d\mathbf{v}_p}{dt} = \frac{q}{m_p c} \mathbf{v}_p \times \mathbf{B}, \quad (10)$$

where  $\mathbf{v}_p$  is the PINS velocity (note that  $|\mathbf{v}_p| = v$ , the speed used in Equations (3) and (12)),  $q$  is the proton charge,  $m_p$  is the proton mass,  $c$  is the speed of light, and  $\mathbf{B}$  is the total (mean  $\mathbf{B}_0$  + turbulent  $\delta\mathbf{B}$ ) magnetic field at the particle's instantaneous position. We integrate Equation (10) using the Bulirsch–Stoer method (Press et al. 2002). We use adaptive stepping to track the error such that it does not exceed a tolerance limit during each step. In the adaptive Bulirsch–Stoer method, the magnetic field is calculated at multiple discrete locations during each

time step in order to render a desired accuracy of a particle's trajectory. For the majority of the results presented in this study, the tolerance is set such that over a typical charge-exchange lifetime of a proton outside the heliopause ( $\sim 2$  yr), the accumulated error in particle energy is  $\lesssim 5\%$ . For results compared to *IBEX* data (Figure 6), we decrease the tolerance level such that the accumulated error in particle energy is  $< 2\%$  over a typical charge-exchange lifetime.

There is a key difference in the methods used in this study to simulate the *IBEX* ribbon compared to, e.g., GJ15. While those authors initialized millions of protons extracted from a neutral SW distribution outside the heliopause and propagated the particles forward in time until they charge-exchange into secondary ENAs, in this study we propagate particles backwards in time, similar to the methodology described by Zirnstein et al. (2018), which we summarize here. We step outward from the Sun along an *IBEX* line of sight in small, discrete intervals  $\Delta r$  (the distance interval for the ENA integration, see Equation (12)). At each step outside the heliopause, we begin an integration of Equation (10) backward in time starting from the current position  $\mathbf{r}$ , which is the position at which a secondary ENA with the desired speed and propagation direction would intersect *IBEX*'s line of sight. We integrate Equation (10) from  $t = 0$  to  $t_{\max}$ , where  $t_{\max} > \tau_{\text{ex}} = (n_H \sigma_{\text{ex}} v)^{-1}$  and  $\tau_{\text{ex}}$  is the charge-exchange mean free lifetime. For this study we set  $t_{\max} = 2\tau_{\text{ex}}$ . Note, however, that the probability for conversion of ions to ENAs follows an exponential charge-exchange distribution. Therefore, we employ a weighting function that accounts for the exponential probability by acting as a normalized amplitude for ENA creation. This is described below.

During each time step  $\Delta t$  of the integration of Equation (10) from  $t = 0$  to  $t_{\max}$  (where we set  $\Delta t$  equal to the inverse gyrofrequency  $\Omega_g^{-1} = m_p/(qB)$ ), we record the current velocity vector of the proton  $\mathbf{v}'$  at current position  $\mathbf{r}'$  and calculate the local production of PINS (at  $\mathbf{r}'$  with velocity  $\mathbf{v}'$ ) by charge-exchange using the neutral SW distribution from Section 2.2. The contribution of these PINS to the secondary ENA flux back at the start position ( $\mathbf{r}$ ,  $t = 0$ ) (see Equations (13) and (14)) is weighted by the probability for these PINS to survive traveling back to ( $\mathbf{r}$ ,  $t = 0$ ). This weighting is given by (Zirnstein et al. 2015b)

$$W(t) = \frac{\exp(-t/\tau_{\text{ex}})}{\int_0^{t_{\max}} \exp(-t'/\tau_{\text{ex}}) dt'}, \quad (11)$$

which we normalize such that the integral of  $W(t)$  from  $t = 0$  to  $t_{\max}$  equals 1. The form for  $W(t) \propto \exp(-t/\tau_{\text{ex}})$  represents the charge-exchange lifetime of the particle, which drops exponentially over time. We calculate  $\tau_{\text{ex}}$  once at  $t = 0$  for computational simplicity. This is a reasonable assumption because most PINS do not travel far during their lifetime ( $< 10$  au), which is much smaller than the scale over which the interstellar neutral density changes significantly (e.g., Heerikhuisen et al. 2014). The application of Equation (11) implies that the farther away from ( $\mathbf{r}$ ,  $t = 0$ ) that a PINS originates, the less likely it is to contribute to secondary ENAs created at ( $\mathbf{r}$ ,  $t = 0$ ).

After computing the contribution of PINS to the secondary ENA flux at ( $\mathbf{r}$ ,  $t = 0$ ), for distance interval  $\Delta r$ , we take another step outward along the *IBEX* line of sight and repeat

**Table 1**  
Turbulence Spectrum Parameters for Each Model Case Presented in This Study

Parameter:	Outer Correlation Scale, $L_C$ (pc (au))	Variance rms at $L_C$ , $\sigma_C$ ( $\mu\text{G}$ )	Spectrum Wavelength Upper Limit, $\lambda_U$ (au)	Variance rms at $\lambda_U$ , $\sigma_U$ ( $\mu\text{G}$ )	Spectrum Wavelength Lower Limit, $\lambda_L$ (au)
Case 1	0.015 ( $3.1 \times 10^3$ )	4	10	0.28	$3.5 \times 10^{-5}$
Case 2	0.015 ( $3.1 \times 10^3$ )	4	50	0.48	$3.5 \times 10^{-5}$
Case 3	0.015 ( $3.1 \times 10^3$ )	4	100	0.60	$3.5 \times 10^{-5}$
Case 4	0.015 ( $3.1 \times 10^3$ )	4	500	1.0	$3.5 \times 10^{-5}$

the process described above. We repeat this process until we reach the outer boundary of the simulation, which we set as 600 au from the Sun.

The equation for the secondary ENA differential flux from PINS outside the heliopause is given by

$$J_{\text{ENA}}(\Omega, v) = \frac{v^2}{m_p} \int_{r_{\text{HP}}}^{r_{\text{OB}}} f_0(\mathbf{r}, v) n_{\text{H}}(\mathbf{r}) \sigma_{\text{ex}} P(\mathbf{r}, v) d\mathbf{r}, \quad (12)$$

where  $\Omega$  is the *IBEX* line-of-sight direction,  $f_0$  is the PINS distribution,  $P$  is the ENA survival probability (discussed below),  $r_{\text{HP}}$  is the distance to the heliopause in direction  $\Omega$  (extracted from our MHD simulation), and  $r_{\text{OB}} = 600$  au is the outer boundary. The PINS distribution is given by

$$f_0(\mathbf{r}, v) = \int_0^{t_{\text{max}}} W(t) [S_{\text{NSW}}(\mathbf{r}, v) \tau_{\text{ex}}] dt, \quad (13)$$

where  $S_{\text{NSW}}$  is the PINS source function produced by charge-exchange of the neutral SW outside the heliopause. We take into account the fact that the neutral SW distribution has a finite, though small, thermal spread transverse to the radial direction. Based on typical SW conditions, the transverse temperature of the neutral SW at the termination shock,  $T_{\text{t,TS}}$ , is approximately  $5 \times 10^3$  K, which drops off as  $r^{-2}$  farther from the Sun due to expansion (Florinski & Heerikhuisen 2017). Therefore, the PINS source function is given by

$$S_{\text{NSW}}(\mathbf{r}, v) = \frac{I_{\text{NSW}}(\mathbf{r}, v) m_p}{2\pi} n_p(\mathbf{r}) \sigma_{\text{ex}} v \times \left[ \frac{1}{\pi \delta v_t^2(r)} e^{-\left(\frac{v_t}{\delta v_t(r)}\right)^2} H(90^\circ - \cos^{-1}(\hat{\mathbf{v}}_p \cdot \hat{\mathbf{r}})) \right],$$

$$v_t = v \sin(\cos^{-1}(\hat{\mathbf{v}}_p \cdot \mathbf{r})),$$

$$\delta v_t(r) = \sqrt{\frac{2k_B T_{\text{t,TS}}}{m_p} \left(\frac{r_{\text{TS}}}{r}\right)^2}, \quad (14)$$

where the last term in square brackets for  $S_{\text{NSW}}$  represents the transverse component of the neutral SW distribution. We apply the Heaviside step function ( $H$ ) because PINS can only be created in the same hemisphere as the radially propagating neutral SW.

We also include the survival probability for ENAs,  $P(\mathbf{r}, v)$ , traveling from their point of creation to the SW termination shock in Equation (12). We exclude the survival probability inside the termination shock to make our results directly comparable with *IBEX* data corrected for survival probability (e.g., McComas et al. 2017). Unlike our previous work, we do not integrate Equation (12) over the *IBEX-Hi* energy ranges, due to the computational cost of simulating the propagation of

many particles at different energies. However, in Figure 6 where we compare to *IBEX* data, we include the *IBEX-Hi* angular collimator response (Funsten et al. 2009) in the model results.

### 3. Results

In this section we present results from simulating ribbon ENA fluxes at 1 au from a source of PINS propagating in turbulence outside the heliopause. We also present results for different turbulence parameters (Table 1).

#### 3.1. Uniform versus Draped Mean ISMF, $\mathbf{B}_0$

First, we simulate the ribbon in a uniform mean ISMF with a turbulent component. We assume that the mean field,  $\mathbf{B}_0$ , is directed toward ( $227^\circ 28', 34^\circ 62'$ ) in ecliptic J2000 coordinates, which is the pristine ISMF direction far from the heliosphere derived by Zirnstein et al. (2016), and set  $|\mathbf{B}_0| = 4 \mu\text{G}$ . Note that we choose  $|\mathbf{B}_0| = 4 \mu\text{G}$  (and not  $2.93 \mu\text{G}$ , which was derived as the magnitude of the pristine/unaffected ISMF magnitude far from the heliosphere) in order to simulate the effects of a stronger, compressed mean field, similar to what happens to the ISMF draped around the heliopause, and also to emulate a magnitude similar to that used by GJ15. We also show results for the case of a self-consistently compressed and draped mean ISMF,  $\mathbf{B}_0 = \mathbf{B}_{\text{MHD}}$ , where  $\mathbf{B}_{\text{MHD}}$  is directly taken from our MHD simulation of the heliosphere using the best-fit parameters derived by Zirnstein et al. (2016). Results comparing these two cases are shown in Figure 3, alongside the case without turbulence.

As shown in Figure 3, the uniform mean ISMF assumption produces a significantly narrower ribbon than in the case where the ISMF drapes around the heliosphere. The draping bends the  $\mathbf{B}_0 \cdot \mathbf{r} = 0$  surface and naturally widens the angular portion of the sky that produces ENAs visible at 1 au (e.g., Pogorelov et al. 2011; Zirnstein et al. 2015a, 2016, 2019). The ribbon in the uniform mean ISMF case is also narrower than in the uniform mean ISMF case presented by GJ15, likely because we limit the size of large-scale modes to  $< 500$  au. We show results for  $\lambda_U = 10$  and 500 au (see Figure 2 and Table 1). For small  $\lambda_U$ , the uniform field case produces a ribbon that follows a great circle in the sky. For large  $\lambda_U$ , the turbulence power at large scales changes the mean field direction and causes the ribbon to meander across the sky, away from the great circle. The draped mean field case shows the effect of large-scale turbulence ( $\lambda_U = 500$  au) on the ribbon's position and structure in the sky. Note also that turbulence at both scales widens the ribbon (compared to the right panel in Figure 3), since it allows particles at a broader range of pitch angles to have directions preferentially aligned with *IBEX*'s line of sight.

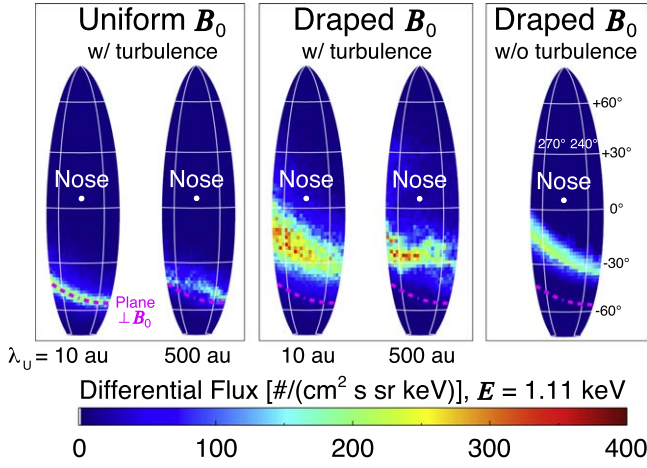


**Figure 3.** Model ribbon partial-sky maps at 1.1 keV for Cases 1 ( $\lambda_U = 10$  au) and 4 ( $\lambda_U = 500$  au) in Table 1, with turbulence superposed on a uniform mean field  $\mathbf{B}_0$  (left box) or a draped mean field derived from the MHD simulation ( $\mathbf{B}_0 = \mathbf{B}_{\text{MHD}}$ ) (middle box). We also show the case where there is no turbulence (right box). The plane perpendicular to the (uniform)  $\mathbf{B}_0$  direction is shown as the dashed magenta curve, which is the same in each panel. Longitude and latitude lines are labeled in the rightmost map. The pixel resolution of each map is  $2^\circ \times 2^\circ$ .

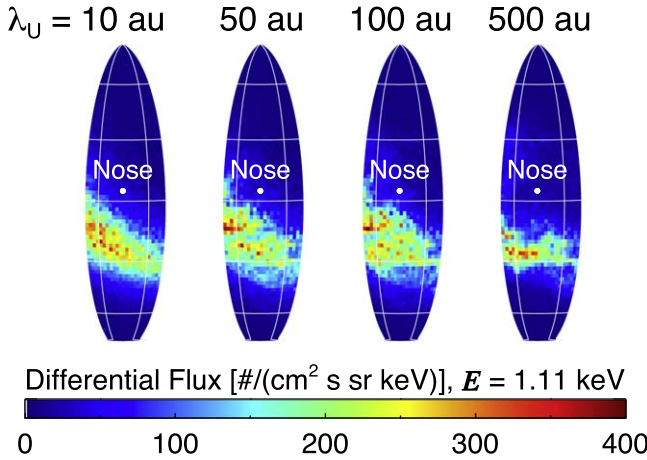


**Figure 4.** Model ribbon partial-sky maps at 1.1 keV for different spectrum upper limits,  $\lambda_U$  (Cases 1–4 in Table 1) and a draped mean field  $\mathbf{B}_0$ . Each case uses a turbulence spectrum that is normalized to *Voyager 1* observations of power spectral density shown in Figure 2. We show results for a single turbulence realization. The pixel resolution is  $2^\circ \times 2^\circ$ .

### 3.2. Maximum Turbulence Scale

In this section we show how the ribbon changes when the maximum fluctuation scale size,  $\lambda_U$ , is varied. By varying  $\lambda_U$ , we include or exclude large-scale fluctuations and effectively change (1) the level of magnetic mirroring of particles and (2) the mean field direction. Figure 4 presents results where we varied  $\lambda_U$  between 10 and 500 au, for a single turbulence realization in a draped mean ISMF. Note that “realization” refers to a unique set of random polarizations, phases, and propagation directions of waves in the turbulent magnetic field component. For small  $\lambda_U$ , the full width at half maximum of the ribbon is approximately  $\sim 20^\circ$  and the ribbon structure fluctuates on small scales ( $< 10^\circ$ ), reminiscent of fine-scale structure possibly seen in the first *IBEX* maps (McComas et al. 2009b). As  $\lambda_U$  increases, the ribbon structure becomes more distorted and chaotic at larger scales due to the inclusion of larger fluctuations in the magnetic field with larger amplitudes.

For  $\lambda_U = 500$  au, the peak of the ribbon meanders around the sky and is not consistent with the position or structure of the *IBEX* ribbon.

The results presented in Figure 4 are only for one unique realization of the turbulence, and the ribbon structure may vary for different realizations, where each realization is constructed from a different set of random polarizations, phases, and wavevector directions. The dependence of the ribbon structure on the turbulence realization is demonstrated in more detail in Figure 5, which shows the simulated ribbon for three different turbulence realizations for  $\lambda_U = 50$  au and  $\lambda_U = 500$  au. For the smaller  $\lambda_U$  case, while the different realizations change the small-scale structure and intensities, the large-scale structure remains roughly consistent. On the other hand, for  $\lambda_U = 500$  au, the ribbon at large scales changes drastically. In the first case, the ribbon appears almost parallel to the latitude  $= -30^\circ$  line. For the second case, the ribbon is highly inclined with respect to the ecliptic plane. The large differences are due to the change in the large-scale fluctuations, which change the direction of the draped mean ISMF and alter the directions in the sky in which the large-scale ribbon appears.

The results in Figures 4 and 5, when compared to multi-year averaged *IBEX* observations (see Figure 6), strongly suggest that the draped mean ISMF can be significantly altered by strong, large-scale turbulence in the VLISM, which affects the large-scale structure of the observed *IBEX* ribbon as shown in Figure 5 for  $\lambda_U = 500$  au. A comparison of our simulation for small  $\lambda_U$  (e.g.,  $\lambda_U = 10$  au) with multi-year averaged *IBEX* observations is shown in Figure 6.

In Figure 6, we complete the simulation for the forward hemisphere of the sky (centered near the nose direction) for the case  $\lambda_U = 10$  au and Realization #1. We also show the simulated sky map after implementing the angular smoothing effects of the *IBEX* collimator (Funsten et al. 2009). The model compares reasonably well to the observations, in particular the width and position of the ribbon. Note, however, that we show the total intensity of *IBEX* observations, which includes the globally distributed fluxes emanating from the inner heliosheath that are not included in our simulation. While it appears that our simulation overestimates the observed intensities, it is possible that a different realization of the turbulent field would yield a lower overall intensity in the ribbon (see Figure 5). Our simulation also does not directly account for any time dependence in the ribbon source, and we do not integrate over *IBEX*’s energy response function, both of which may affect the simulated ribbon intensity.

### 3.3. Particle Pitch Angle Distribution in Turbulence

The results presented in this study show that the level of turbulence observed by *Voyager 1* and the maximum scale of the fluctuations significantly affect the propagation of particles outside the heliopause and their ability to produce ENAs that are visible by *IBEX*. In this section we further investigate the distribution of particles in the turbulence configurations presented so far.

Here, we perform a simple test particle simulation (see Figure 7) using the same Bulirsch–Stoer algorithm and turbulence realizations used in the results presented in Sections 3.1 and 3.2. We define a uniform mean field  $\mathbf{B}_0$  to be aligned with the  $z$ -axis with magnitude  $|\mathbf{B}_0| = 4 \mu\text{G}$  and superpose the turbulent field component  $\delta\mathbf{B}$  from the  $\lambda_U = 10$  au and  $\lambda_U = 500$  au cases shown in Figure 4.



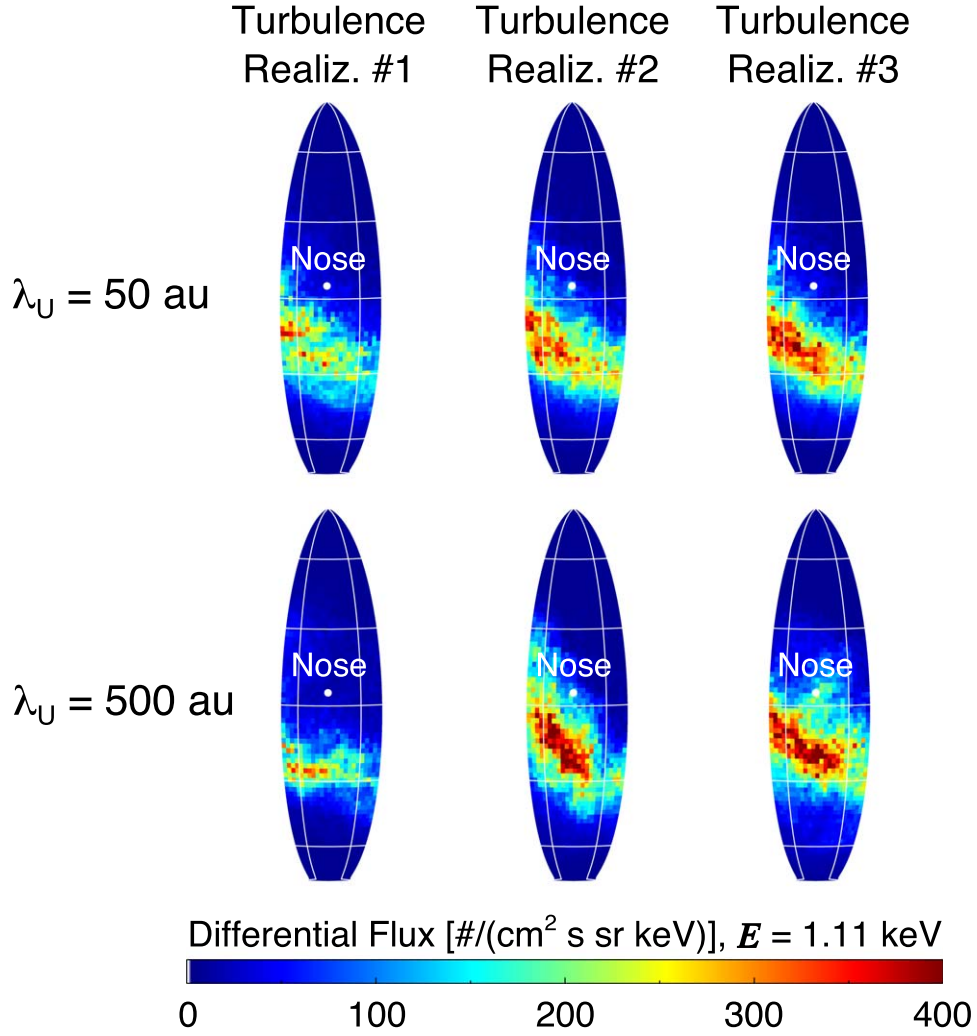


**Figure 5.** Model ribbon partial-sky maps at 1.1 keV for  $\lambda_U = 50$  and 500 au, from three different turbulence spectrum realizations. Note that “Realization #1” is the same as Figure 4. The pixel resolution is  $2^\circ \times 2^\circ$ .

We follow  $\sim 50,000$  particles with radial speed  $400 \text{ km s}^{-1}$ . They are initially randomly distributed in a spherical grid with coordinates  $(r, \theta, \varphi)$  limited to the following ranges:  $100 \text{ au} < r < 1000 \text{ au}$ ,  $-\sin(30^\circ) < \cos(\theta) < \sin(30^\circ)$ ,  $-30^\circ < \varphi < 30^\circ$ . Note that we only release particles in an angular window with opening angle of  $60^\circ$  centered on the  $x$ -axis to improve counting statistics near the radial direction perpendicular to the mean field,  $\mathbf{B}_0 \cdot \mathbf{r} = 0$  (or latitude  $\theta = 0^\circ$ ). Then, as the particles propagate through space, we bin their pitch angle cosine,  $\mu = \cos(\mathbf{v}_p \cdot \mathbf{B}/|\mathbf{B}|)$ , and position every inverse gyrofrequency  $\Omega_g^{-1} = m_p c / (q B_0)$ . The lifetime of each particle,  $t$ , is randomly selected from an exponential distribution,  $\exp(-t/\tau)$ , with a  $1/e$  mean lifetime  $\tau = 500,000$  gyroperiods (1 gyroperiod  $= 2\pi\Omega_g^{-1}$ ). In a  $4 \mu\text{G}$  magnetic field, 500,000 gyroperiods corresponds to approximately 2.5 yr. The  $1/e$  charge-exchange lifetime of a 1.1 keV proton outside the heliopause, assuming an interstellar neutral hydrogen density of  $0.15 \text{ cm}^{-3}$ , is also approximately 2.5 yr.

Figures 8 and 9 show the particle pitch angle distributions for the same turbulence realizations shown in Figure 4 when  $\lambda_U = 10 \text{ au}$  and  $\lambda_U = 500 \text{ au}$ . Note that we bin particles for any radial distance  $r$ , limited to  $|\varphi| < 5^\circ$ , into different latitude ( $\theta$ ) bins. At  $\theta = 0^\circ$ , which is directed toward  $\mathbf{B}_0 \cdot \mathbf{r} = 0$  (to mimic where the center of the ribbon peak would be located),

the pitch angle distribution shows a single peak at  $\mu = 0$ . This is in contrast to the results presented by GJ15, who showed a double-peaked pitch angle distribution in the center of the ribbon (see below). The distribution becomes broader for  $\lambda_U = 500 \text{ au}$  as particles experience a stronger mirror force from the larger fluctuations (and their larger amplitudes), causing the distribution to spread over a larger region of pitch angles around  $90^\circ$ . This effectively creates a wider ribbon, or even a change in the ribbon’s position in the sky (see Figures 3 and 5).

Regarding the existence of the double-humped pitch angle distribution (and double-humped ribbon), we have studied this discrepancy carefully and have found that the double-humped feature is an artifact of the numerical method used by GJ15 and is not real. GJ15 made an unreported modification to the Bulirsch–Stoer numerical integration method, which had the effect of forcing the magnetic field to be constant over a very small, but finite, fraction of each particle’s orbit. The modification was used in order to speed up the calculation, which is otherwise extremely computationally expensive. We have performed several tests using a much smaller and more computationally tractable physical domain to study this. We find that when we use the same modification (constant field over a small portion of the orbit) we obtain the double-humped

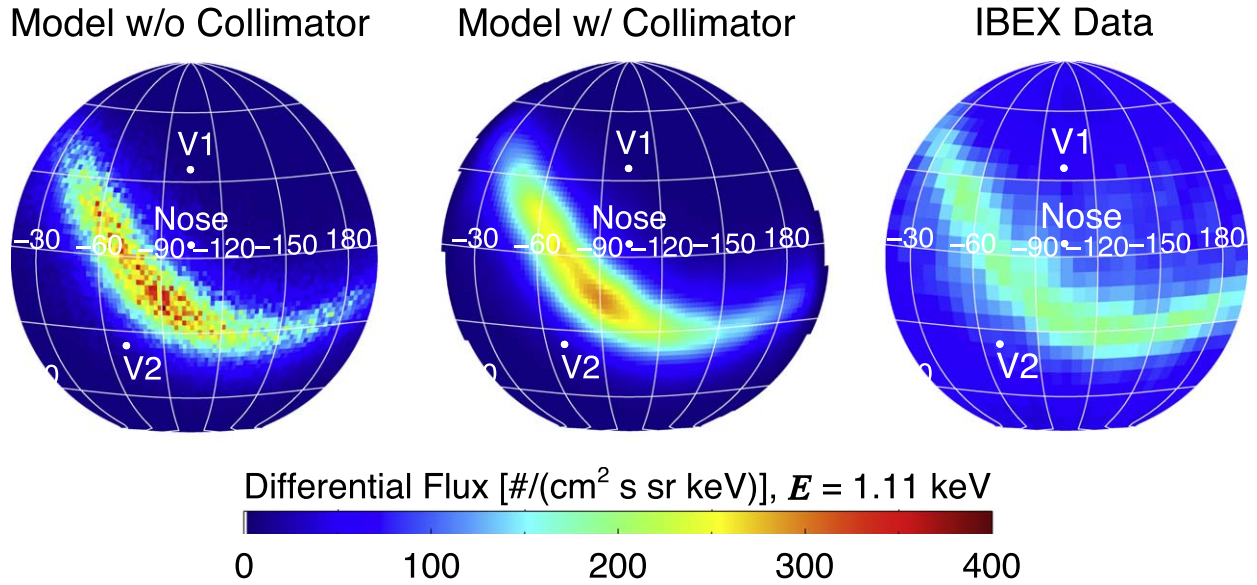


**Figure 6.** Model ribbon partial-sky maps at 1.1 keV for  $\lambda_U = 10$  au and Realization #1. For this result, we decreased the mover tolerance such that the error in energy of a 1.1 keV particle over a typical charge-exchange lifetime ( $\sim 2$  yr) is  $< 2\%$ . We show the model without the angular collimator response of the *IBEX* instrument (left), with the collimator response (middle), and *IBEX* data averaged over 5 yr (right) from McComas et al. (2014). Note that the *IBEX* data also include the globally distributed flux, in particular from pixels near the nose of the heliosphere (e.g., Schwadron et al. 2018). The pixel resolution of the model maps is  $2^\circ \times 2^\circ$ , while the resolution of the *IBEX* map is  $6^\circ \times 6^\circ$ .

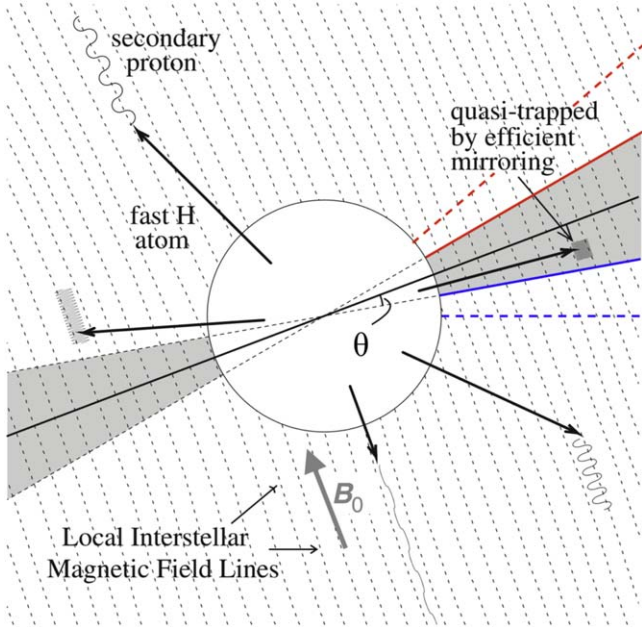


**Figure 7.** Illustration of the test particle system used to compute particle pitch angle distributions in Section 3.3. The directions in the sky from which the pitch angle distributions are extracted from are shown as the solid black ( $\theta = 0^\circ$ ), solid red and blue ( $\theta = +10^\circ$  and  $-10^\circ$ ) and dashed red and blue ( $\theta = +20^\circ$  and  $-20^\circ$ ) lines. Adapted from GJ15.

pitch angle distribution; but when we relax this assumption, the double-humped feature goes away. Thus, we conclude that the double-humped feature presented by GJ15 is not real.

At larger angles from  $\mathbf{B}_0 \cdot \mathbf{r} = 0$  ( $\theta = \pm 10^\circ$ ), the pitch angle distributions become broader in both cases, and double-peaked for the  $\lambda_U = 10$  au case, due to the mirroring of particles into backward-propagating hemispheres. This is similar to the results presented by GJ15, supporting the importance of the magnetic mirror force's impact on the source particle distribution of the ribbon. For  $\theta = \pm 20^\circ$ , the pitch angle

distribution becomes less symmetric about pitch angle  $90^\circ$ , with more particles propagating in the forward hemisphere (away from  $\mathbf{B}_0 \cdot \mathbf{r}$ ). This is because, at this larger angle from  $\mathbf{B}_0 \cdot \mathbf{r} = 0$ , fewer particles have mirrored due to their smaller initial pitch angles (or larger  $\mu$ ). The results for  $\lambda_U = 10$  au and  $\lambda_U = 500$  au are qualitatively similar, though the peaks in the pitch angle distributions are more broadly spread out for the  $\lambda_U = 500$  au case due to enhanced mirroring from larger fluctuations in  $\delta \mathbf{B}$ .

#### 4. Discussion and Conclusions

In this study we simulated the transport of PINS outside the heliopause in the presence of Kolmogorov-like, homogeneous, and isotropic turbulence with a power spectrum consistent with *Voyager 1* observations and a draped mean ISMF inferred from *IBEX* ENA observations. We tested the effects of the assumption of a uniform mean ISMF versus a draped mean ISMF derived from our MHD simulation of the heliosphere, as well as how different turbulence realizations and maximum fluctuation scales affect the ribbon fluxes at 1 au. In the following we discuss the implications of our results for the source of the ribbon and the turbulence properties in the VLISM.

##### 4.1. Turbulence Fluctuation Scale outside the Heliopause

The Kolmogorov-like turbulence that is observed by *Voyager 1* in the VLISM at scales  $< 5$  au is significantly stronger than the expected pristine turbulence from the interstellar medium (see Figure 2), suggesting that it is not just of interstellar origin. We find that in order to reproduce the large-scale structure of the *IBEX* ribbon (McComas et al. 2017), under the assumptions of our model, the turbulence observed by *Voyager 1* should remain limited to length scales  $\lambda_U \lesssim 50$  au. We find that the cases where  $\lambda_U \lesssim 50$  au, such as the simulation for  $\lambda_U \sim 10$  au shown in Figure 6, produce the most realistic solutions. This turbulence could either be a result



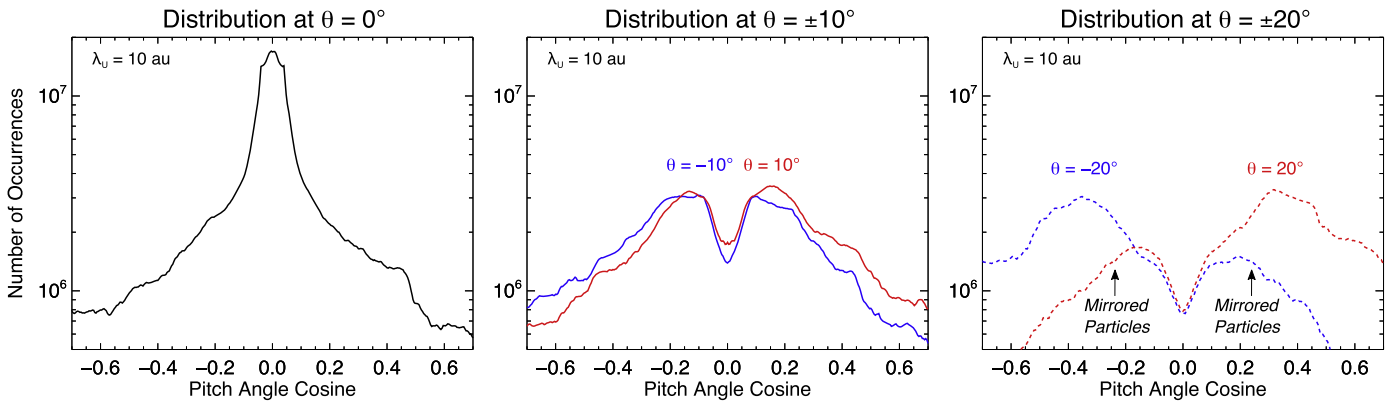


**Figure 8.** Particle pitch angle distribution in uniform mean ISMF ( $B_0$  directed toward  $+z$ -axis) using the same turbulence field  $\delta B$  from Figure 6 ( $\lambda_U = 10$  au, Realization #1, Case 1 from Table 1). The directions in the sky from which the distributions are extracted are shown in Figure 7.

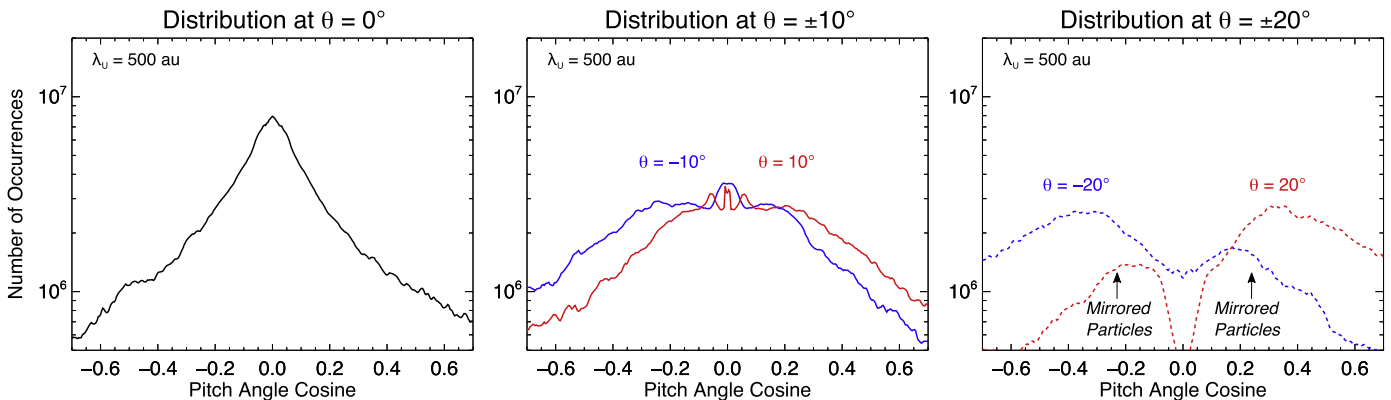


**Figure 9.** Same as Figure 8, except for different turbulence parameters ( $\lambda_U = 500$  au, Realization #1, Case 4 from Table 1).

of the interaction between the heliosphere and the pristine interstellar turbulence or it could be entirely of heliospheric origin. For example, Zank et al. (2017) showed that the largely compressive fluctuations observed by *Voyager 1* from  $\sim 2013.4$  to 2014.6 (Burlaga et al. 2015) are consistent with fast-mode waves propagating outside the heliopause, originating from fast- and slow-mode waves that were refracted at the heliopause and propagated outside it at highly oblique angles to the ISMF. However, subsequent observations by *Voyager 1* showed that from  $\sim 2015.4$  to 2016.7 the fluctuations were dominantly transverse to the mean field and not compressive, though the uncertainty of this result was large (Burlaga et al. 2018; see also Fraternale et al. 2019). As suggested by Burlaga et al. (2018), these observations can be verified by future *Voyager 1* and 2 observations of the VLISM turbulence.

Nevertheless, Zank et al. (2017) predict that locally generated turbulence from fast-mode waves emanating from the heliosphere is likely superposed on the spectrum of pristine interstellar turbulence. The dependence of this superposed turbulence spectrum on distance from the heliosphere, however, is not well understood, which is the reason why in our study we assumed that the turbulence power spectrum was the same everywhere outside the heliopause. While this assumption can be analyzed in more detail in a future study, we believe that our results are robust since the spatial distribution of the ribbon source is largely concentrated within a few tens of au from the heliopause (e.g., Zirnstein et al. 2019) where, presumably, the turbulence observed by *Voyager 1* is strongest.

#### 4.2. Ribbon Structure: Single or Double Peak?

The results presented in this study show that the double-peaked ribbon feature predicted by GJ15 does not exist, at least not for the particular properties of turbulence presented in this study (circularly polarized, homogeneous, and isotropic turbulence). The reason for this was discussed above in Section 3.3. Instead, the ribbon is single-peaked, but still slightly broadened due to the magnetic mirroring of particles in turbulence. However, the breadth of the ribbon is a combination of (1) the draping of the ISMF around the heliopause and (2) the interaction of particles with turbulence resulting in either magnetic mirroring or pitch angle scattering. This is apparent by comparing the simulation results between a uniform mean ISMF and a draped mean ISMF with and without turbulence (Figure 3).

Through our analysis of the discrepancy in the results presented here and those presented in GJ15 regarding the existence of the double-humped feature, we have found that the shape of the ribbon ENA emission profile near  $90^\circ$  pitch angle can vary significantly depending on the nature of the turbulence. It remains an open question as to whether a double-peaked ribbon might arise for different turbulence properties. Under the assumption that the normalization of the turbulence power is consistent with *Voyager 1* observations (Figure 2), and assuming that the turbulence is isotropic and Kolmogorov-like, we doubt that a double-peaked ribbon is likely, especially in a draped mean ISMF, which would smear out any double-peaked structure.

### 4.3. Fine Structure in the Ribbon

While the existence of the double-peaked ribbon appears unlikely based on the results presented in this study, it may be possible that smaller fine structure exists in the ribbon, like that possibly observed in the first *IBEX* maps (McComas et al. 2009b). Our simulation results (e.g., Figure 6) suggest that neighboring pixels separated by a few degrees may differ in intensity due to particle interactions with turbulence. Moreover, evolution of these intensities over time can be expected. The time over which ENA fluxes evolve depends on the turnover time of turbulent eddies at the scales over which we are observing.

For example, at the *IBEX* angular resolution of  $6.5^\circ$  (Funsten et al. 2009), and with a ribbon source distance of approximately 150 au from the Sun (Swaczyna et al. 2016a; Zirnstein et al. 2018, 2019), the arc distance of the ribbon's source with this opening angle corresponds to 16 au. The turnover time for turbulence with wavelength  $\lambda = 16$  au is approximately proportional to the ratio of wavelength to the Alfvén speed outside the heliopause,  $\lambda/v_A$ . In a  $4 \mu\text{G}$  magnetic field and plasma density of  $0.1 \text{ cm}^{-3}$ ,  $v_A = 28 \text{ km s}^{-1}$ . Thus, the turnover time is of the order of  $\lambda/v_A = 16 \text{ au}/28 \text{ km s}^{-1} \cong 2.7 \text{ yr}$ . While it is not certain which scales of turbulence the PINS are most sensitive to, we can estimate that the PINS may interact with turbulent eddies that change on timescales of the order of a few years. However, it is possible that small changes in turbulent eddies in a particular direction of the sky, and thus small changes in the pitch angles of particles, may affect ENA fluxes just enough to be observed at 1 au by *IBEX*. Therefore, it is possible that the expected time over which fine structure in the ribbon changes is less than a few years. Suppose the turbulent eddy turnover time results in, on average, a change in phase of  $90^\circ$ . A small change in phase ( $\lesssim 10^\circ$ ) over a period of a few months could change the particle pitch angles enough to have an observable change in ENA flux at 1 au. Note that these timescales are significantly smaller than the quasi-periodic, 11 yr solar cycle, but similar to more frequent changes in the SW caused by, e.g., merged interaction regions and shocks propagating to the outer heliosphere.





The statistical significance of the fine structure shown in our results is questionable. The results presented in this study show simulated ENA fluxes in  $2^\circ \times 2^\circ$  bins. While the trajectories of protons are simulated to high accuracy, we only simulate protons whose final ENA trajectories intersect the center of each bin. Therefore, it is possible that if we simulated protons with trajectories intersecting other areas of each bin, the average ENA fluxes in the bins might be different. To test this, we computed the angular power spectrum of the simulated map shown in Figure 6 (“Model w/o Collimator”) to determine the angular scales at which the fine structure is consistent with statistical noise. We find that the power spectrum flattens at multipole  $>20$  (or angular scales  $<180^\circ/20 = 9^\circ$ ), suggesting that at angular scales  $<10^\circ$  the fine structure might be statistical noise. However, it may partly be attributed to the protons' interactions with turbulence. This behavior can produce random-like fine structure at these scales if the protons' trajectories are stochastic before they become ENAs.

We also note that while the argument on the validity of the fine structure from our simulation is speculative, it is also a potentially important hypothesis that can be tested by the upcoming *Interstellar Mapping and Acceleration Probe* (*IMAP*). The angular scales at which we see fine structure in

the ribbon, the amount the fine structure will change over time, over how long, and whether *IBEX* has sufficient measurement statistics to observe these changes are not currently well understood. However, *IMAP* will have better angular resolution than *IBEX*, between  $4^\circ$  for *IMAP-Hi* and  $2^\circ$  for *IMAP-Ultra*, as well as better statistics and higher temporal resolution (McComas et al. 2018a). With these improvements, *IMAP* could better observe and quantify fine structure in the ribbon and fluctuations in the fine structure corresponding to the evolution of small turbulent eddies outside the heliopause.

E.Z., M.D., and J.H. acknowledge support from NASA grant 80NSSC17K0597. This work was also partly funded by the *IBEX* mission as a part of the NASA Explorer Program (80NSSC18K0237). J.G. acknowledges NASA grant NNX15AJ71G and useful discussions on this topic with J.R. Jokipii. R.K. acknowledges support from the Max-Planck/Princeton Center for Plasma Physics and NSF Grant No. AST-1517638. E.Z. and J.G. acknowledge helpful discussions at the team meeting “The Physics of the Very Local Interstellar Medium and Its Interaction with the Heliosphere” supported by the International Space Science Institute in Bern, Switzerland. E.Z. thanks Len Burlaga for providing the power spectral density data from *Voyager 1*. The work reported in this paper was partly performed at the TIGRESS high performance computer center at Princeton University, which is jointly supported by the Princeton Institute for Computational Science and Engineering and the Princeton University Office of Information Technology's Research Computing department.

### ORCID iDs

E. J. Zirnstein  <https://orcid.org/0000-0001-7240-0618>  
 R. Kumar  <https://orcid.org/0000-0003-1925-8469>  
 D. J. McComas  <https://orcid.org/0000-0001-6160-1158>  
 M. A. Dayeh  <https://orcid.org/0000-0001-9323-1200>  
 J. Heerikhuisen  <https://orcid.org/0000-0001-7867-3633>

### References

- Batchelor, G. K. 1960, *The Theory of Homogeneous Turbulence* (2nd ed.; Cambridge: Cambridge Univ. Press)
- Burlaga, L. F., Florinski, V., & Ness, N. F. 2015, *ApJL*, **804**, L31
- Burlaga, L. F., Florinski, V., & Ness, N. F. 2018, *ApJ*, **854**, 20
- Bzowski, M., Kubiak, M. A., Czechowski, A., & Grygorczuk, J. 2017, *ApJ*, **845**, 15
- Bzowski, M., Möbius, E., Tarnopolski, S., Izmodenov, V., & Gloeckler, G. 2009, *SSRv*, **143**, 177
- Bzowski, M., Sokół, J. M., Tokumaru, M., et al. 2013, in *Cross-Calibration of Far UV Spectra of Solar System Objects and the Heliosphere*, ed. E. Quémerais, M. Snow, & R.-M. Bonnet (New York: Springer), 67
- Chalov, S. V., Alexashov, D. B., McComas, D., et al. 2010, *ApJL*, **716**, L99
- Desai, M. I., Dayeh, M. A., Allegrini, F., et al. 2019, *ApJ*, **875**, 91
- Florinski, V., & Heerikhuisen, J. 2017, *ApJ*, **838**, 50
- Florinski, V., Heerikhuisen, J., Niemiec, J., & Ernst, A. 2016, *ApJ*, **826**, 197
- Florinski, V., Zank, G. P., Heerikhuisen, J., Hu, Q., & Khazanov, I. 2010, *ApJ*, **719**, 1097
- Fraternali, F., Pogorelov, N. V., Richardson, J. D., & Tordella, D. 2019, *ApJ*, **872**, 40
- Funsten, H. O., Allegrini, F., Bochsler, P., et al. 2009, *SSRv*, **146**, 75
- Fuselier, S. A., Bochsler, P., Chornay, D., et al. 2009, *SSRv*, **146**, 117
- Gamayunov, K., Zhang, M., & Rassoul, H. 2010, *ApJ*, **725**, 2251
- Gamayunov, K. V., Heerikhuisen, J., & Rassoul, H. 2017, *ApJ*, **845**, 63
- Gamayunov, K. V., Heerikhuisen, J., & Rassoul, H. 2019, *ApJL*, **876**, L21
- Giacalone, J., & Jokipii, J. R. 1999, *ApJ*, **520**, 204
- Giacalone, J., & Jokipii, J. R. 2015, *ApJL*, **812**, L9
- Gloeckler, G., Möbius, E., Geiss, J., et al. 2004, *A&A*, **426**, 845

- Grygorczuk, J., Ratkiewicz, R., Strumik, M., & Grzedzielski, S. 2011, *ApJL*, **727**, L48
- Gurnett, D. A., Kurth, W. S., Burlaga, L. F., & Ness, N. F. 2013, *Sci*, **341**, 1489
- Heerikhuisen, J., & Pogorelov, N. V. 2011, *ApJ*, **738**, 29
- Heerikhuisen, J., Pogorelov, N. V., Florinski, V., Zank, G. P., & Kharchenko, V. 2009, in ASP Conf. Ser. 406, Numerical Modeling of Space Plasma Flows: ASTRONUM-2008, ed. N. V. Pogorelov et al. (San Francisco, CA: ASP), 189
- Heerikhuisen, J., Pogorelov, N. V., Zank, G. P., et al. 2010, *ApJL*, **708**, L126
- Heerikhuisen, J., Pogorelov, N. V., & Zank, G. P. 2013, in ASP Conf. Ser. 474, Numerical Modeling of Space Plasma Flows, ASTRONUM-2012, ed. N. V. Pogorelov, E. Audit, & G. P. Zank (San Francisco, CA: ASP), 195
- Heerikhuisen, J., Zirnstein, E. J., Funsten, H. O., Pogorelov, N. V., & Zank, G. P. 2014, *ApJ*, **784**, 73
- Isenberg, P. A. 2014, *ApJ*, **787**, 76
- Isenberg, P. A. 2015, *JPCS*, **577**, 012014
- Isenberg, P. A., Forbes, T. G., & Möbius, E. 2015, *ApJ*, **805**, 153
- Kubiak, M. A., Swaczyna, P., Bzowski, M., et al. 2016, *ApJS*, **223**, 25
- Lallement, R., Quémerais, E., Koutroumpa, D., et al. 2010, in AIP Conf. Ser. 1216, Twelfth International Solar Wind Conference, ed. M. Maksimovic et al. (Melville, NY: AIP), 555
- Lee, M. A., Fahr, H. J., Kucharek, H., et al. 2009, *SSRv*, **146**, 275
- Lindsay, B. G., & Stebbings, R. F. 2005, *JGR*, **110**, A12213
- McComas, D. J., Allegrini, F., Bochsler, P., et al. 2009a, *SSRv*, **146**, 11
- McComas, D. J., Allegrini, F., Bochsler, P., et al. 2009b, *Sci*, **326**, 959
- McComas, D. J., Allegrini, F., Bzowski, M., et al. 2014, *ApJS*, **213**, 20
- McComas, D. J., Bzowski, M., Fuselier, S. A., et al. 2015, *ApJS*, **220**, 22
- McComas, D. J., Christian, E. R., Schwadron, N. A., et al. 2018a, *SSRv*, **214**, 116
- McComas, D. J., Dayeh, M. A., Funsten, H. O., et al. 2018b, *ApJL*, **856**, L10
- McComas, D. J., Zirnstein, E. J., Bzowski, M., et al. 2017, *ApJS*, **229**, 41
- Möbius, E., Bochsler, P., Bzowski, M., et al. 2009, *Sci*, **326**, 969
- Möbius, E., Liu, K., Funsten, H., Gary, S. P., & Winske, D. 2013, *ApJ*, **766**, 129
- Niemiec, J., Florinski, V., Heerikhuisen, J., & Nishikawa, K.-I. 2016, *ApJ*, **826**, 198
- Park, J., Kucharek, H., Möbius, E., et al. 2016, *ApJ*, **833**, 130
- Pogorelov, N. V., Borovikov, S. N., Zank, G. P., & Ogino, T. 2009a, *ApJ*, **696**, 1478
- Pogorelov, N. V., Heerikhuisen, J., Zank, G. P., et al. 2011, *ApJ*, **742**, 104
- Pogorelov, N. V., Heerikhuisen, J., Zank, G. P., & Borovikov, S. N. 2009b, *SSRv*, **143**, 31
- Pogorelov, N. V., Zank, G. P., Borovikov, S. N., et al. 2008, in ASP Conf. Ser. 385, Numerical Modeling of Space Plasma Flows, ed. N. V. Pogorelov, E. Audit, & G. P. Zank (San Francisco, CA: ASP), 180
- Press, W. H., Teukolsky, S. A., Vetterling, W. T., & Flannery, B. P. 2002, Numerical Recipes in C: The Art of Scientific Computing (2nd ed.; Cambridge: Cambridge Univ. Press)
- Ratkiewicz, R., Strumik, M., & Grygorczuk, J. 2012, *ApJ*, **756**, 3
- Schwadron, N. A., Allegrini, F., Bzowski, M., et al. 2018, *ApJS*, **239**, 1
- Schwadron, N. A., Bzowski, M., Crew, G. B., et al. 2009, *Sci*, **326**, 966
- Schwadron, N. A., & McComas, D. J. 2013, *ApJ*, **764**, 92
- Schwadron, N. A., Möbius, E., McComas, D. J., et al. 2016, *ApJ*, **828**, 81
- Sokół, J. M., Bzowski, M., & Tokumaru, M. 2019, *ApJ*, **872**, 57
- Sokół, J. M., Swaczyna, P., Bzowski, M., & Tokumaru, M. 2015, *SoPh*, **290**, 2589
- Stone, E. C., Cummings, A. C., McDonald, F. B., et al. 2013, *Sci*, **341**, 150
- Strumik, M., Ben-Jaffel, L., Ratkiewicz, R., & Grygorczuk, J. 2011, *ApJL*, **741**, L6
- Summerlin, E. J., Viñas, A. F., Moore, T. E., Christian, E. R., & Cooper, J. F. 2014, *ApJ*, **793**, 93
- Swaczyna, P., Bzowski, M., Christian, E. R., et al. 2016a, *ApJ*, **823**, 119
- Swaczyna, P., Bzowski, M., & Sokół, J. M. 2016b, *ApJ*, **827**, 71
- Zank, G. P. 1999, *SSRv*, **89**, 413
- Zank, G. P. 2015, *ARA&A*, **53**, 449
- Zank, G. P., Du, S., & Hunana, P. 2017, *ApJ*, **842**, 114
- Zirnstein, E. J., Heerikhuisen, J., & Dayeh, M. A. 2018, *ApJ*, **855**, 30
- Zirnstein, E. J., Heerikhuisen, J., Funsten, H. O., et al. 2016, *ApJL*, **818**, L18
- Zirnstein, E. J., Heerikhuisen, J., & McComas, D. J. 2015a, *ApJL*, **804**, L22
- Zirnstein, E. J., Heerikhuisen, J., Pogorelov, N. V., McComas, D. J., & Dayeh, M. A. 2015b, *ApJ*, **804**, 5
- Zirnstein, E. J., Heerikhuisen, J., Zank, G. P., et al. 2017, *ApJ*, **836**, 238
- Zirnstein, E. J., McComas, D. J., Schwadron, N. A., et al. 2019, *ApJ*, **876**, 92